ISSN 2278-2540 | DOI: 10.51583/IJLTEMAS | Volume XV, Issue XI, November 2026

Field Thermal Performance and Modelled Energy Yield of Four 100 W Polycrystalline PV Modules on Different Mounting Substrates in Arusha, Tanzania

Nickson John Malima[1]*, Urbanus F. Melkior[1]

[1]Electrical Engineering Department, Arusha Technical College, Arusha, Tanzania

DOI: https://doi.org/10.51583/IJLTEMAS.2026.151100057

Received: 09 November 2026; Accepted: 14 November 2026; Published: 26 November 2026

ABSTRACT

Photovoltaic (PV) modules in equatorial highland climates operate far above the 25 °C reference of Standard Test Conditions (STC), and the mounting substrate is one of the few variables an installer can still choose after procurement. Four 100 W polycrystalline silicon modules were monitored on four substrates in Arusha, Tanzania (3.4° S, 1 400 m a.s.l.): a bare corrugated metal sheet roof (CMSR), a colour-coated roof sheet, a pole-mounted rack and a concrete slab. Back-surface temperature, ambient conditions and irradiance were logged at 1 min intervals. Under about 1010 W m^{-2} and 31.2 °C ambient, mean module temperatures were 61.7 °C (CMSR), 59.7 °C (pole), 54.4 °C (coated sheet) and 45.0 °C (concrete, reconstructed by regression). The most robust result, a synchronous paired test, showed the concrete-slab module running 10.3 K cooler than the coated-sheet module (95 % CI 8.9–11.8 K under conservative autocorrelation). Translating temperatures through $\gamma = -0.41$ % K^{-1} gives thermal losses of 15.1, 14.2, 12.1 and 8.2 %, a 7.9 % energy advantage of the slab over the bare roof (8.4 % with a temperature-scaled single-diode model). Field-effective NOCT fell 1.9–16.1 K below declared values. Because each module occupied one substrate, module and mounting effects are partly confounded, and wind speed and electrical output were not measured; the results are therefore presented as strong field evidence that warrants replicated, rotated-assignment trials with anemometry and measured electrical output.

Keywords: photovoltaic module temperature; mounting configuration; corrugated metal roof; nominal operating cell temperature; single-diode model; tropical highland climate.

Nomenclature

Symbol	Description	Unit	Symbol	Description	Unit
A	Module aperture area	m^2	P_{mp}	Maximum power	W
E	Delivered energy	Wh	PR_{th}	Thermal performance ratio	–
FF, FF_0	Fill factor; ideal fill factor	–	R_s, R_{sh}	Series, shunt resistance	Ω
G	Plane-of-array irradiance	W m^{-2}	$R_{s,eq}$	Green lumped resistance bound	Ω
I_0, I_{ph}	Saturation, photo-current	A	T_a, T_m	Ambient, module temperature	°C
I_{sc}, I_{mp}	Short-circuit, MPP current	A	U	Overall heat-loss coefficient	W m^{-2} K^{-1}

ISSN 2278-2540 | DOI: 10.51583/IJLTEMAS | Volume XV, Issue XI, November 2026

k_R	Ross coefficient	K m^2 W^{-1}	V_{oc}, V_{mp}	Open-circuit, MPP voltage	V
n	Diode ideality factor	–	V_t	Module thermal voltage	V
n_{eff}	Effective sample size	–	α, β, γ	Coefficients of I_{sc}, V_{oc}, P_{mp}	% K^{-1}
N_s	Cells in series	–	NOCT	Nominal operating cell temperature	°C

1. INTRODUCTION

Polycrystalline (multicrystalline) silicon remains common in the small off-grid and rooftop segments of sub-Saharan African markets because of its low cost per watt and mature supply chain. Module ratings, however, refer to Standard Test Conditions (STC: 1000 W m^{-2}, 25 °C cell temperature, AM1.5G), a combination that rarely occurs in an equatorial highland climate. In Arusha, at about 1 400 m on the southern slopes of Mount Meru, midday plane-of-array irradiance frequently exceeds 1000 W m^{-2} while air temperature at module height exceeds 30 °C in the warm February interval. With a maximum-power temperature coefficient near −0.4 % K^{-1}, a module at 65 °C loses about one sixth of its nameplate output before soiling, mismatch or wiring losses are considered (Dwivedi et al., 2020; Santiago et al., 2018).

The thermal derating of PV modules is well documented. Santiago et al. (2018) compared twenty module-temperature models, from the linear Ross relation to wind-dependent forms, and showed that the choice of model alone changes estimated annual temperature losses appreciably. The Faiman heat-loss model is now adopted in IEC 61853-2 (IEC, 2016), and it is implemented together with the Sandia array performance model in open-source simulation tools (Holmgren et al., 2018; Prilliman et al., 2020). The relations linking fill factor, series resistance and the diode equation are set out by Smets et al. (2016), and datasheet-based five-parameter single-diode models are still being refined (Lo Brano, 2026; Malik et al., 2025; Mlazi et al., 2024). Ogbomo et al. (2017) reviewed module technologies for tropical climates.

The mounting configuration is a recognized first-order driver of module temperature. Sandia mounting coefficients distinguish open-rack, close-roof and insulated-back installations (Holmgren et al., 2018; Prilliman et al., 2020), and Kaplanis et al. (2022) quantified the effects of wind and inclination on free-standing, building-applied and building-integrated modules. Long-term monitoring in Switzerland found building-integrated modules running 20–30 °C hotter than identical open-rack modules (Oezkalay et al., 2022). Kempe et al. (2023) related rooftop standoff to the 98th-percentile temperature that triggers higher-temperature qualification under IEC TS 63126 (IEC, 2025), and Pretorius and Nielsen (2024) showed in South Africa that configuration-specific heat-loss factors changed simulated annual yield by about 3 %. In tropical settings, Yadav et al. (2025) reported cell temperatures up to 64 °C on a North Indian rooftop, with temperature responsible for a 9.6 % output decline and convective loss 16.19 % higher than in a simulated ground-mounted system. Mohamad Radzi et al. (2025) documented the seasonality of module temperature in Malaysian arrays, Rajani et al. (2026) showed measurable power gains from 5–10 K cooling of a bifacial PV-thermal system, and Kurnia (2026) confirmed that the temperature coefficient governs module ranking in hot conditions. In East Africa, Adamu et al. (2024) found in Nairobi that the energy advantage of MPPT charge controllers almost vanished at high cell temperatures, a direct consequence of thermal voltage collapse in small systems.

Most of this evidence comes from temperate sites, utility plants or building-integrated systems. Side-by-side field comparisons of the substrates used for small systems in East Africa remain scarce. Here small systems are commonly fixed close to corrugated metal sheet roofs, which are cheap and ubiquitous, while pole racks and concrete slabs are usually chosen for structural or security reasons rather than thermal ones. This study addresses that gap with simultaneous field measurements in Arusha. Its objectives are: (i) to characterize the four modules at STC with a consistent five-parameter single-diode model; (ii) to quantify the difference in

ISSN 2278-2540 | DOI: 10.51583/IJLTEMAS | Volume XV, Issue XI, November 2026

operating temperature between the four module–substrate pairs, with an explicit assessment of statistical robustness; (iii) to derive field-effective Ross coefficients, heat-loss coefficients and NOCT values; (iv) to estimate the consequences for power, energy and performance ratio with two independent translation models; and (v) to state the practical implications and the conditions under which they can be generalized.

2. MATERIALS AND METHODS

2.1 Site and climate

Measurements were made in Arusha, northern Tanzania (approximately 3.4° S, 36.7° E, 1 400 m a.s.l.). The site lies in a temperate highland tropical climate (Köppen Cwb) grading into tropical savanna (Aw) at lower elevations, with long rains from March to May and short rains from October to December. February lies in the warm, comparatively dry interval between the two rainy seasons and provides the clear-sky, high-irradiance conditions that represent the thermal worst case. At 1 400 m the standard atmospheric pressure is about 86 % of the sea-level value, so the air density and, with it, the convective heat-transfer coefficient at a given wind speed are reduced (Duffie et al., 2020). In February the solar declination (about −15° to −8°) places the noon sun slightly south of the zenith at this latitude.

2.2 Modules under test

Four commercially available 100 W polycrystalline silicon modules from different manufacturers were used. Each is a 36-cell series string (N_s = 36), consistent with declared open-circuit voltages of 21.5–22.2 V. Their declared characteristics are listed in Table 1. P1 and P2 are higher-current, lower-voltage devices; P3 and P4 trade current for voltage. Because each module was permanently assigned to one substrate, every comparison in this paper is between module–substrate pairs; this design limitation is addressed explicitly in Sections 2.6 and 5.

Table 1: Declared STC characteristics and mounting assignment.

Characteristic	P1	P2	P3	P4
Maximum power, P_{mp} (W)	100	100	100	100
Open-circuit voltage, V_{oc} (V)	21.62	21.53	22.14	22.16
Voltage at MPP, V_{mp} (V)	18	17.7	18.5	18.4
Short-circuit current, I_{sc} (A)	6.31	6.22	5.78	5.8
Current at MPP, I_{mp} (A)	5.63	5.72	5.43	5.5
Declared NOCT (°C)	46 ± 2	47 ± 2	47 ± 2	47 ± 2
Mounting substrate	Bare CMSR	Coated sheet	Pole rack	Concrete slab

CMSR = corrugated metal sheet roof (uncoated galvanized steel).

2.3 Mounting configurations

- **P1 – bare CMSR.** Close-coupled to uncoated galvanized corrugated sheet with a nominal 70 mm standoff. Galvanized steel has high solar absorptance relative to its low thermal emittance, so it runs hot;

ISSN 2278-2540 | DOI: 10.51583/IJLTEMAS | Volume XV, Issue XI, November 2026

its low emittance also reflects much of the module's own rear-face infrared emission back to the module.

- **P2 – green colour-coated sheet.** Same geometry and standoff as P1, but the factory paint gives the sheet a high thermal emittance, changing the radiative exchange with the module rear face without changing the convective geometry.
- **P3 – pole-mounted rack.** Carried on a single mast two meters above ground, with both faces exposed to ambient air; nominally the open-rack geometry assumed in NOCT testing.
- **P4 – concrete slab.** Mounted with a nominal 70 mm standoff above a concrete apron of high thermal mass and high emittance.

All modules faced north (equatorward) at 14° tilt angle and were cleaned before each measurement day. Figure 1 summarizes the configurations.

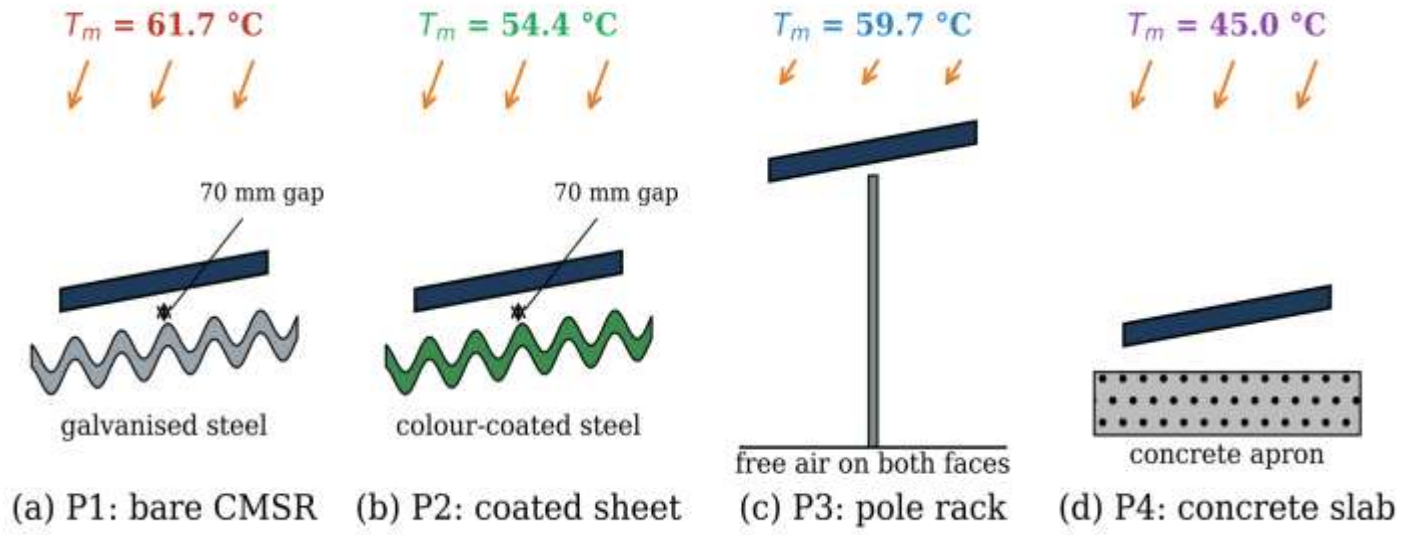


Figure 1: Mounting configurations and campaign-mean module back-surface temperatures.

2.4 Instrumentation and campaigns

Module back-surface temperature was measured with USB SSN-11e bonded to the centre of each rear laminate, the proxy for cell temperature recommended by IEC 61724-1 (IEC, 2021b). No cell-to-back offset was applied (typically 1–3 K at 1000 W m^{-2}; Santiago et al., 2018). Ambient temperature, relative humidity and dew point were logged with USB SSN-22e at module height. Irradiance was measured with USB TES 132 solar power meter, nominally coplanar with the modules. The four data sets are summarized in Table 2.

Table 2: Measurement campaigns.

Campaign	Date	Window (EAT)	Records	Purpose
A	9-Feb	10:36–15:24	1 min	P1 with exposed and shaded roof-sheet temperatures
B	10-Feb	10:36–14:24	1 min, n = 229	P1, P2, P3, ambient, RH, dew point, G

ISSN 2278-2540 | DOI: 10.51583/IJLTEMAS | Volume XV, Issue XI, November 2026

C	9-Feb	10:30–16:27	1 min, n = 357	Paired P2 and P4 (synchronous)
D	9-Feb	10:45–15:01	1 Hz, n = 15 303	Irradiance regime

The concrete-slab module (P4) was monitored only on 9 February. To place it in the four-way comparison of 10 February, its temperature was reconstructed from the coated-sheet module (P2), which was logged on both days, by ordinary least squares fitted to the 229 overlapping minutes of Campaign C:

$$T_{m,P4} = 15.380 + 0.5437\, T_{m,P2} \quad (r = 0.739, \text{RMS residual } 1.66 \text{ K}) \tag{1}$$

A slope below unity reflects the larger thermal inertia of the slab installation; a constant-offset transfer produced physically impossible values below ambient. The reconstructed P4 series is therefore a model estimate, not a measurement: it shares the variability of the P2 series and is used only descriptively in Sections 3.4–3.8. The substrate effect for P4 is tested independently with the synchronous data of Campaign C (Section 3.9).

2.5 Mathematical formulation

2.5.1 Single-diode model

Each module is represented by the five-parameter equivalent circuit

$$I = I_{ph} - I_0[\exp((V + IR_s)/V_t) - 1] - (V + IR_s)/R_{sh} \tag{2}$$

$$V_t = n\, N_s\, k\, T_c / q \tag{3}$$

with $k = 1.380649 \times 10^{-23}$ J K^{-1} and $q = 1.602177 \times 10^{-19}$ C. Equation (2) is implicit in I and was solved by Brent bracketing.

2.5.2. STC descriptors

From the datasheet quadruple:

$$P_{mp} = V_{mp} I_{mp}, \quad FF = P_{mp}/(V_{oc} I_{sc}), \quad \eta_{STC} = P_{mp}/(A\, G_{STC}), \quad R_{ch} = V_{oc}/I_{sc} \tag{4}$$

In Eq. (4), P_{mp} is the product of the declared V_{mp} and I_{mp}, not the nameplate rating. For P1 this gives 18.0 V × 5.63 A = 101.34 W, 1.34 % above the nominal 100 W; P2–P4 give 101.24, 100.45 and 101.20 W (Table 3). The difference is not a computational error. The 100 W nameplate is a nominal power class to which the manufacturer's power tolerance applies, whereas V_{mp} and I_{mp} are measured values rounded to the last digit shown (±0.05 V and ±0.005 A, about ±0.4 W in the product). Products of 100.45–101.34 W therefore lie within the power tolerance commonly declared for modules of this class (e.g. 0 to +3 % or ±3 %). To keep the maximum-power point, the fill factor and the single-diode parameters (Eqs. 5–10) mutually consistent, the computed product, not the nameplate value, is used as $P_{mp,STC}$ in Eqs. (13) and (14) and in Tables 3 and 8. Using 100 W instead would lower every absolute power and energy value by 0.45–1.34 %, would leave the thermal losses and PR_{th} unchanged ($P_{mp,STC}$ cancels in Eq. 14), and would shift the inter-module energy gains of Table 8 by less than one percentage point without changing their ranking.

Green's empirical expression (Smets et al., 2016) gives the fill factor of a loss-free device with normalised open-circuit voltage $v_{oc} = V_{oc}/V_t$:

$$FF_0 = [v_{oc} - \ln(v_{oc} + 0.72)]/(v_{oc} + 1) \tag{5}$$

$$r_s = 1 - FF/FF_0, \quad R_{s,eq} = r_s R_{ch} \tag{6}$$

ISSN 2278-2540 | DOI: 10.51583/IJLTEMAS | Volume XV, Issue XI, November 2026

Equation (6) attributes the entire fill-factor deficit to series resistance (infinite shunt). $R_{s,eq}$ is therefore an upper bound on R_s, not an estimate of it.

2.5.3 Parameter extraction

The datasheet supplies four conditions – the short-circuit, open-circuit and maximum-power points and $dP/dV = 0$ at the MPP – for five unknowns:

$$I_{sc} = I_{ph} - I_0[\exp(I_{sc}R_s/V_t) - 1] - I_{sc}R_s/R_{sh} \quad (7)$$

$$0 = I_{ph} - I_0[\exp(V_{oc}/V_t) - 1] - V_{oc}/R_{sh} \quad (8)$$

$$I_{mp} = I_{ph} - I_0[\exp((V_{mp} + I_{mp}R_s)/V_t) - 1] - (V_{mp} + I_{mp}R_s)/R_{sh} \quad (9)$$

$$I_{mp} + V_{mp}(dI/dV)_{mp} = 0, \quad (dI/dV)_{mp} = -g_m/(1 + R_s g_m) \quad (10)$$

where $g_m = (I_0/V_t)\exp[(V_{mp} + I_{mp}R_s)/V_t] + 1/R_{sh}$. The system was closed by fixing the ideality factor, which is the least identifiable parameter from datasheet data (Lo Brano, 2026; Mlazi et al., 2024). A common value n = 1.00 was adopted for all four modules because it is the largest value for which an exact solution with finite R_{sh} exists for every module: P4 admits exact solutions only for $n \leq 1.025$, whereas P1 admits them up to $n = 1.44$. The same n is used in Eq. (5), so Tables 3 and 4 are mutually consistent. Equations (7)–(10) were solved by bounded trust-region least squares from nine starting points; residuals were below 10^{-13} A. Sensitivity to datasheet rounding was assessed by perturbing V_{mp} by ±0.05 V and I_{mp} by ±0.005 A.

2.5.4 Translation to field conditions

Two independent translations were used. Model I is the linear temperature-coefficient form (consistent in structure with IEC 60891 (IEC, 2021a), but not its Procedure 1, which requires measured I–V curves), with literature values for p-Si: $\alpha = +0.05$ % K^{-1}, $\beta = -0.33$ % K^{-1}, $\gamma = -0.41$ % K^{-1}:

$$I_{sc} = I_{sc,STC}(G/G_{STC})[1 + \alpha(T_m - 25)] \quad (11)$$

$$V_{oc} = V_{oc,STC}[1 + \beta(T_m - 25)] + V_t \ln(G/G_{STC}) \quad (12)$$

$$P_{mp} = P_{mp,STC}(G/G_{STC})[1 + \gamma(T_m - 25)] \quad (13)$$

In Eqs. (11)–(13) the coefficients, quoted above in % K^{-1}, are converted to decimal fractions per kelvin by dividing by 100: $\alpha = +0.05$ % K^{-1} = $+5.0 \times 10^{-4}$ K^{-1}, $\beta = -0.33$ % K^{-1} = -3.3×10^{-3} K^{-1} and $\gamma = -0.41$ % K^{-1} = -4.1×10^{-3} K^{-1}. T_m is in °C, so $(T_m - 25)$ is a temperature difference in K. $I_{sc,STC}$ and $V_{oc,STC}$ are the declared values of Table 1, $P_{mp,STC}$ is the product of Eq. (4) (Table 3) and G_{STC} = 1000 W m^{-2}. In Eq. (12), V_t is the module thermal voltage of Eq. (3) evaluated at the field temperature, $V_t = n\,N_s\,k\,(T_m + 273.15)/q$, with n = 1.00, N_s = 36 and the back-surface temperature taken as the cell temperature (Section 2.4). Because it includes N_s, it is a module-level quantity: 1.039 V for P1 at 61.70 °C and 0.987 V for P4 at 44.97 °C, compared with 25.7 mV for a single cell at 25 °C. As a worked example, for P1 at G = 1010 W m^{-2} and T_m = 61.70 °C, Eq. (13) gives $P_{mp} = 101.34 \times 1.010 \times [1 - 0.0041 \times 36.70] = 86.95$ W and Eq. (12) gives $V_{oc} = 21.62 \times [1 - 0.0033 \times 36.70] + 1.039 \times \ln(1.010) = 19.01$ V, the values listed in Table 8.

Model II is the temperature-scaled single-diode model of De Soto, as implemented in pvlib (Holmgren et al., 2018), applied to the parameters of Table 4: I_{ph} scales with G and α; $I_0 \propto T^3 \exp[-E_g/(kT)]$ with $E_g = 1.121$ eV $(1 - 0.0002677\,\Delta T)$; $V_t \propto T$; R_s is constant and $R_{sh} \propto 1/G$. Model II implies $\beta = -0.37$ to -0.39 % K^{-1} and $\gamma = -0.44$ to -0.46 % K^{-1}, within the published range for p-Si, and therefore serves as a physically based cross-check on Model I. Energy and the thermal performance ratio are

$$E = \int P_{mp}\,dt, \quad PR_{th} = E / [P_{mp,STC} \int (G/G_{STC})\,dt] \quad (14)$$

ISSN 2278-2540 | DOI: 10.51583/IJLTEMAS | Volume XV, Issue XI, November 2026

In Eq. (14), P_{mp} is in W and time t is in hours, so E is in Wh; G/G_{STC} is dimensionless, and the bracketed denominator is the loss-free reference energy E_{ref} (Wh). Both integrals were evaluated with the trapezoidal rule over the 1 min records, i.e. with a time step Δt = 1 min = 1/60 h; the 229 samples of Campaign B span 228 intervals, or 3.8 h.

Because only temperature is modelled, PR_{th} captures thermal loss alone and is not the full IEC 61724-1 performance ratio.

2.5.5 Thermal characterization

At fixed wind speed the steady-state energy balance reduces to the Ross relation, from which an effective NOCT and the equivalent overall heat-loss coefficient follow:

$$T_m - T_a = k_R G, \quad \mathrm{NOCT}_{eff} = 20 + 800\, k_R, \quad U = 1/k_R \tag{15}$$

U corresponds to $U_0 + U_1 v$ in the Faiman model (IEC, 2016) at the prevailing wind speed v, which allows direct comparison with published heat-loss factors.

2.6 Statistical treatment

Minute-resolution temperatures are strongly autocorrelated, and each configuration contains a single module, so the 229 minutes of Campaign B are repeated measures of one experimental unit rather than independent samples. Two consequences follow. First, inference about mounting types in general is not possible from these data; the contrasts describe these four installations. Second, naïve t tests overstate significance. For a lag-1

autocorrelation ρ, the effective sample size is approximately $n_{eff} = n(1 - \rho)/(1 + \rho)$ (Wilks, 2019), so ρ = 0.9 reduces 229 minutes to about 12 effective observations. For each of the six Welch contrasts of Campaign B we therefore report the mean difference, Cohen's d, the minimum n_{eff} at which the contrast remains significant after Holm–Bonferroni correction (significance level 0.05), and the adjusted p value at a conservative n_{eff} = 12. The primary test of the substrate effect is the synchronous paired difference of Campaign C, for which confidence intervals are given both for n = 229 and for n_{eff} = 12; a heteroskedasticity- and autocorrelation-consistent estimator (Lazarus et al., 2018) is the recommended refinement once the raw series are re-analysed. Pearson correlation was used for meteorological covariates. Computations used Python 3.12 (NumPy, SciPy, pandas, Matplotlib).

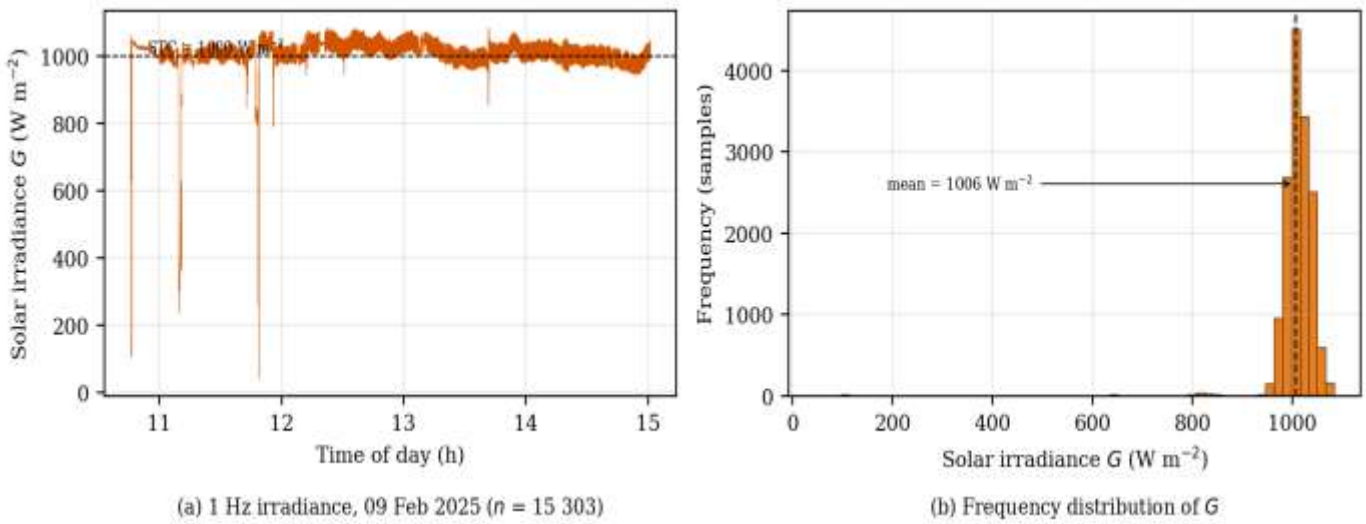
3. RESULTS

3.1 Meteorological conditions

The 1 Hz record of Campaign D (Figure 2) contains 15 303 samples with a mean of 1006 W m^{-2}; 1.78 % of samples fell below 900 W m^{-2} during brief occlusions. During Campaign B, irradiance was 1010 ± 9 W m^{-2}, ambient temperature 31.2 ± 1.8 °C, relative humidity 50.6 ± 5.5 % and dew point 19.6 ± 0.9 °C.

Two features of the irradiance record need caution. First, irradiance stayed within ±3 % across windows extending about two hours either side of solar noon. For a fixed plane, the cosine of the incidence angle alone should have reduced irradiance by roughly 10–15 % at the ends of these windows. The flat record is consistent with the meter being oriented towards the sun rather than held strictly coplanar, or with sensor saturation. Second, all module temperatures fell by up to 20 K at about 13:03 on 10 February (Figure 5) with no corresponding change in the irradiance trace, which points to an unrecorded gust or a time-base offset between loggers. Because irradiance is common to all configurations, these issues affect absolute values of k_R, E_{ref} and PR_{th} more than the comparison between configurations.

ISSN 2278-2540 | DOI: 10.51583/IJLTEMAS | Volume XV, Issue XI, November 2026



(a) 1 Hz irradiance, 09 Feb 2025 (n = 15 303) (b) Frequency distribution of G

Figure 2: Irradiance on test day.

3.2 Electrical characterization at STC

Table 3 lists the STC descriptors. Computed maximum powers lie between 100.45 W and 101.34 W, a spread of less than 1 %, and STC efficiencies (common assumed area 0.6588 m^2) between 15.25 % and 15.38 %. Fill factor separates the modules clearly: P4 (78.74 %) and P3 (78.50 %) exceed P2 (75.60 %) and P1 (74.28 %). With n = 1.00, the loss-free fill factor FF_0 is 0.828–0.832, so the normalized deficit r_s ranges from 5.3 % (P4) to 10.3 % (P1). The corresponding Green bound $R_{s,eq}$ falls from 0.354 Ω (P1) to 0.203 Ω (P4). As explained in Section 2.5, this bound assigns all losses to series resistance; Section 3.3 separates them.

Table 3: STC descriptors from the declared characteristics (Eqs. 4–6, n = 1.00).

Quantity	Unit	P1	P2	P3	P4
Maximum power, P_{mp}	W	101.34	101.24	100.45	101.2
Fill factor, FF	%	74.28	75.6	78.5	78.74
Ideal fill factor, FF_0	–	0.8284	0.8279	0.8314	0.8315
Normalised V_{oc}, v_{oc}	–	23.37	23.28	23.94	23.96
Normalised deficit, r_s	–	0.103	0.087	0.056	0.053
Green bound, $R_{s,eq}$	Ω	0.354	0.301	0.214	0.203
Characteristic resistance, R_{ch}	Ω	3.426	3.461	3.83	3.821
STC efficiency, η_{STC}	%	15.38	15.37	15.25	15.36

ISSN 2278-2540 | DOI: 10.51583/IJLTEMAS | Volume XV, Issue XI, November 2026

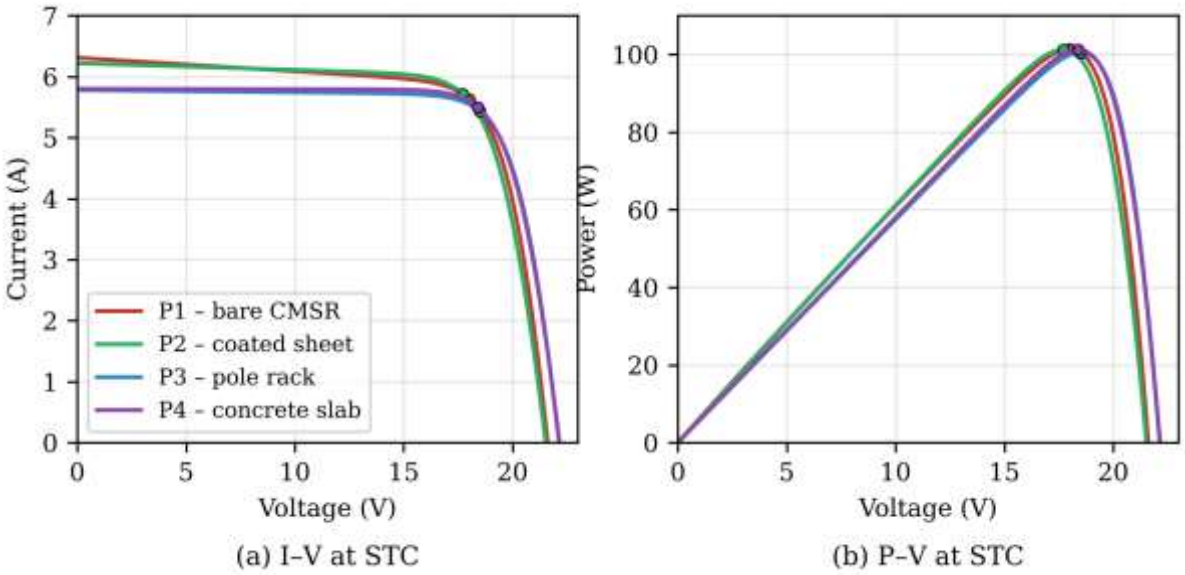


Figure 3: STC markers show declared MPPs.

3.3 Single-diode parameters

Table 4 gives the extracted parameters. With a common ideality factor, the series resistances are similar (0.145–0.190 Ω) and do not follow the fill-factor ranking. The fill-factor differences are instead carried by the shunt resistance, which rises from 45 Ω (P1) through 92 Ω (P2) and 268 Ω (P3) to about 2.3 kΩ (P4). At the STC maximum-power point, shunt dissipation amounts to 7.8 % of output for P1 but only 0.2 % for P4, while series dissipation is 4.5–6.1 % for all four (Figure 11b). The extracted I_{ph} exceeds I_{sc} by 0.32 % (P1), 0.21 % (P2), 0.06 % (P3) and 0.01 % (P4), consistent with the size of the shunt path. The P1 and P2 shunt values are robust to datasheet rounding (44–46 Ω and 89–95 Ω), whereas the P4 value is effectively unbounded (1.2 kΩ to above 10 kΩ): a very high fill factor constrains R_{sh} only from below. The physically meaningful conclusion is that P1's fill-factor deficit is shunt-dominated. Low shunt resistance penalizes a module most at low irradiance, so P1's disadvantage will be larger in the morning, evening and overcast conditions than at the near-STC irradiance of this campaign.

Table 4: Single-diode parameters at STC (n = 1.00; ranges reflect datasheet rounding).

Parameter	Unit	P1	P2	P3	P4
Photocurrent, I_{ph}	A	6.3303	6.2328	5.7834	5.8005
Saturation current, I_0	A	4.13×10^{-10}	4.66×10^{-10}	2.29×10^{-10}	2.28×10^{-10}
Series resistance, R_s	Ω	0.145 (0.135–0.155)	0.190 (0.180–0.199)	0.158 (0.148–0.168)	0.181 (0.171–0.191)
Shunt resistance, R_{sh}	Ω	45 (44–46)	92 (89–95)	268 (243–299)	2265 (>1186)
Series loss at MPP	% P_{mp}	4.5	6.1	4.6	5.4
Shunt loss at MPP	% P_{mp}	7.8	3.8	1.4	0.2

ISSN 2278-2540 | DOI: 10.51583/IJLTEMAS | Volume XV, Issue XI, November 2026

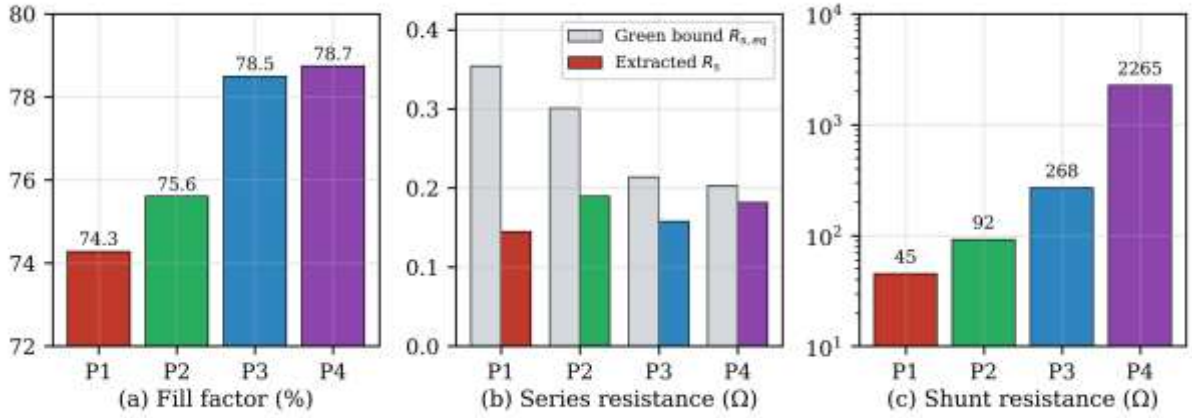


Figure 4: STC descriptors.

3.4 Thermal behaviour of the four configurations

Figure 5 shows the Campaign B records and Table 5 summarizes them. The bare CMSR module was hottest (61.7 ± 5.7 °C), followed by the pole rack (59.7 ± 3.3 °C), the coated sheet (54.4 ± 5.1 °C) and the reconstructed concrete slab (45.0 ± 2.8 °C), corresponding to rises above ambient of 30.5, 28.4, 23.2 and 13.8 K. The directly measured concrete series over the same clock window on 9 February averaged 46.0 ± 2.5 °C, within 1.1 K of the reconstruction.

The pole-mounted module, nominally the best-ventilated case, ran only 2.0 K cooler than the bare roof and 5.2 K hotter than the coated sheet. This contradicts the established ordering, in which open-rack modules run markedly cooler than close-roof modules (Kaplanis et al., 2022; Oezkalay et al., 2022). Reduced air density at 1 400 m cannot explain the anomaly, because it affects all four installations equally. The behaviour of the P3 series is also inconsistent with good ventilation: a free-standing laminate of low thermal mass should respond fastest to gusts, yet P3 showed the narrowest range (50.7–65.1 °C) and barely responded to the 13:03 event that cooled the other modules by 15–20 K (Figure 5). Plausible explanations are a sensor that was insulated or partly detached from the laminate, a logger lag on that channel, a different tilt or azimuth on the mast, or properties of the P3 module itself. None can be excluded without re-measurement, so the pole result is reported as unexplained rather than interpreted physically.

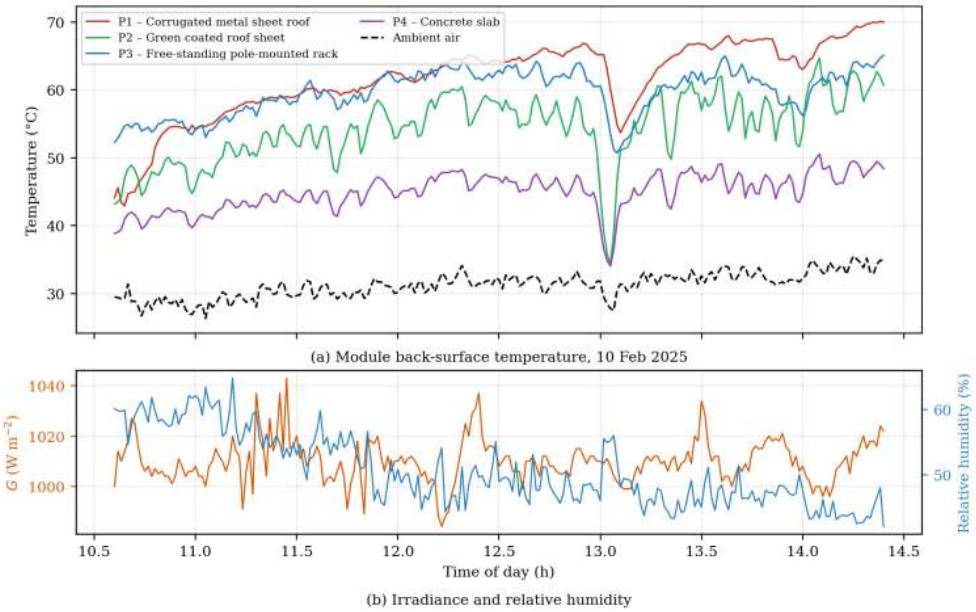


Figure 5: Campaign B parameters.

ISSN 2278-2540 | DOI: 10.51583/IJLTEMAS | Volume XV, Issue XI, November 2026

Table 5: Module temperature statistics, Campaign B (n = 229 min).

Configuration	Module	Mean T_m (°C)	SD (K)	Min (°C)	Max (°C)	$T_m - T_a$ (K)
Bare CMSR	P1	61.7	5.68	42.9	70.1	30.48
Pole rack	P3	59.65	3.35	50.7	65.1	28.43
Coated sheet	P2	54.42	5.05	34.3	64.7	23.2
Concrete slab†	P4	44.97	2.75	34	50.6	13.75

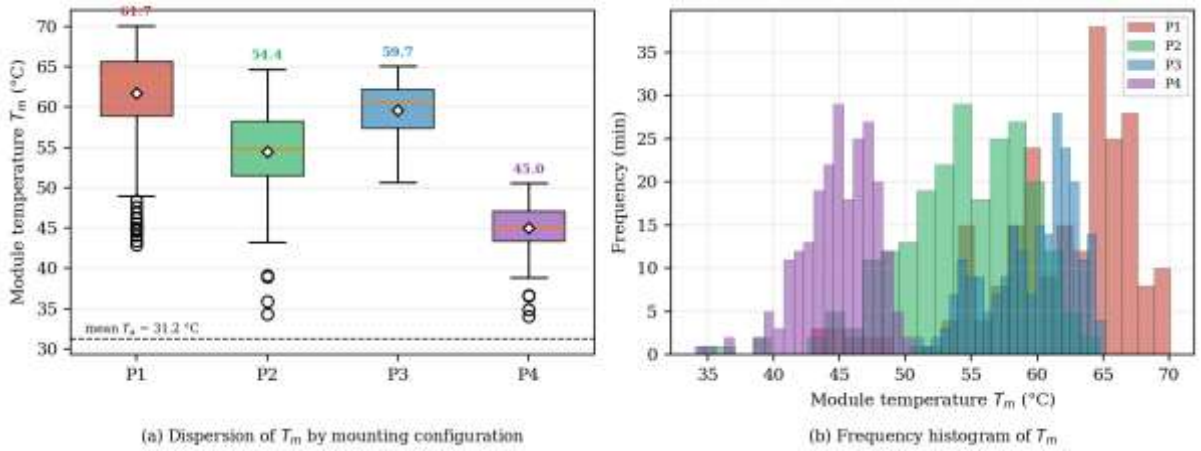


Figure 6: Module temperature distributions plots.

3.5 Robustness of the temperature differences

Table 6 lists the six contrasts. Four are robust: the differences between the concrete slab and every other configuration, and between the coated sheet and the bare roof, remain significant down to n_{eff} of 3–9, well below any plausible effective sample size. The coated-sheet versus pole contrast requires $n_{eff} \geq 9$ and is likely but not certain. The bare-roof versus pole contrast (2.05 K, d = 0.44) requires $n_{eff} \geq 42$, equivalent to a lag-1 autocorrelation below about 0.69, and cannot be considered established. The contrasts involving P4 rely on the reconstructed series; the independent paired test of Section 3.9 confirms that substrate effect.

Table 6: Pairwise temperature contrasts and their robustness to autocorrelation.

Contrast	ΔT (K)	Cohen's d	Min. n_{eff}	Holm p (n_{eff} = 12)	Assessment
P1 − P2 (bare vs coated)	7.28	1.35	9	0.01	Robust
P1 − P3 (bare vs pole)	2.05	0.44	42	0.3	Not established
P1 − P4† (bare vs slab)	16.73	3.75	4	4.7×10^{-7}	Robust
P2 − P3 (coated vs pole)	−5.23	−1.22	9	0.015	Probable

ISSN 2278-2540 | DOI: 10.51583/IJLTEMAS | Volume XV, Issue XI, November 2026

P2 − P4† (coated vs slab)	9.45	2.32	5	1.1×10^{-4}	Robust
P3 − P4† (pole vs slab)	14.68	4.79	3	5.9×10^{-10}	Robust

Min. n_{eff}: smallest effective sample size for Holm-adjusted $p < 0.05$.

Ambient temperature (r = +0.75 to +0.79) and relative humidity (r = −0.71 to −0.80) were the dominant covariates of module temperature; irradiance showed no association (r = +0.05 to +0.08) because it barely varied. The humidity correlation is not causal: air-mass changes that raise humidity also lower dry-bulb temperature.

3.6 Ross coefficients, heat-loss coefficients and field NOCT

Table 7 and Figure 7 give the thermal figures of merit. The Ross coefficient ranges from 0.0136 K m^2 W^{-1} (concrete) to 0.0302 K m^2 W^{-1} (bare roof), and the field-effective NOCT from 30.9 to 44.1 °C, 1.9–16.1 K below the declared 46–47 °C. The bare-roof and pole values lie at the upper end of the range reported for free-standing to flat-roof installations (0.020–0.026; Santiago et al., 2018), as expected for hot midday conditions. The concrete value is lower than any standard mounting class. Its equivalent heat-loss coefficient of 73.5 W m^{-2} K^{-1} would require a wind speed of roughly 7 m s^{-1} in the Faiman model with default coefficients (U_0 = 25, U_1 = 6.84), against PVsyst's open-rack default of 29 W m^{-2} K^{-1} (Pretorius & Nielsen, 2024). Part of the slab's advantage may therefore reflect conductive or radiative coupling to a cool slab that the Ross form does not represent, or sensor placement. Because NOCT is defined for an open rack, datasheet NOCT cannot represent the substrate. The four modules declare almost the same NOCT, yet their field values span 13 K.

Table 7: Field thermal figures of merit (Eq. 15).

Configuration	Module	k_R (K m^2 W^{-1})	U (W m^{-2} K^{-1})	NOCT$_{eff}$ (°C)	Declared (°C)	Deviation (K)
Bare CMSR	P1	0.0302	33.1	44.1	46 ± 2	−1.9
Pole rack	P3	0.0281	35.5	42.5	47 ± 2	−4.5
Coated sheet	P2	0.023	43.5	38.4	47 ± 2	−8.6
Concrete slab†	P4	0.0136	73.5	30.9	47 ± 2	−16.1

Point estimates at $G \approx 1010$ W m^{-2} under the prevailing (unmeasured) wind.

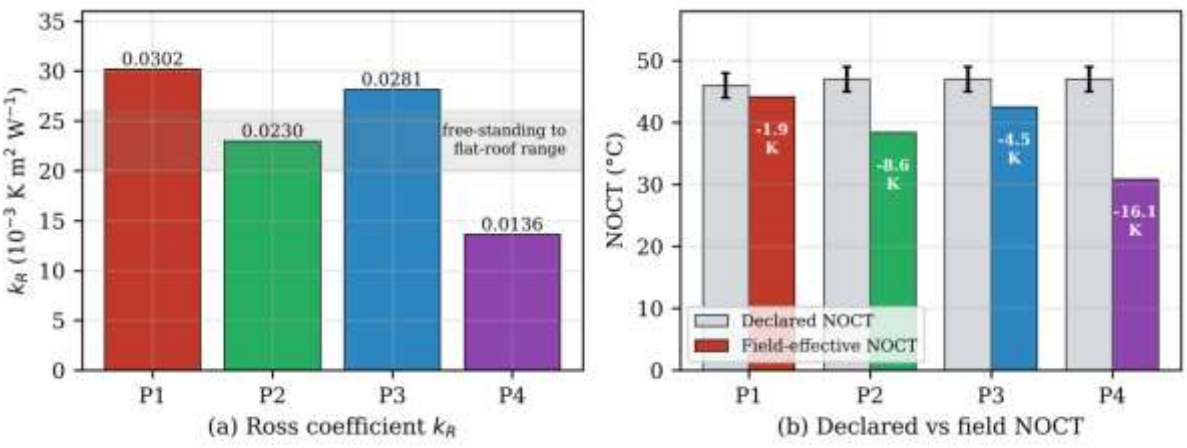


Figure 7: Field Ross coefficients and declared versus field-effective NOCT.

ISSN 2278-2540 | DOI: 10.51583/IJLTEMAS | Volume XV, Issue XI, November 2026

3.7 Translated characteristics and power

Figures 8 and 9 show the characteristics translated to each configuration's mean operating temperature at 1010 W m^{-2}. Short-circuit current rises slightly while open-circuit voltage falls by 6–12 % (Model I) or 7–14 % (Model II). Of the 1.70 V difference in translated V_{oc} between P4 and P1 (Model I), 0.54 V is already present in the datasheets; about 1.2 V is attributable to the higher operating temperature of the roof module. In small 12 V battery systems this thermal voltage collapse, rather than the power loss itself, often decides whether an MPPT controller retains its advantage (Adamu et al., 2024). Mean power at maximum power point is 86.95, 89.92, 87.05 and 93.84 W (Model I) and 85.97, 88.37, 86.05 and 93.15 W (Model II) for P1–P4. The four derating lines in Figure 9 almost coincide, so the separation of the operating points arises from their temperature, i.e. from the module–substrate pair rather than the module rating.

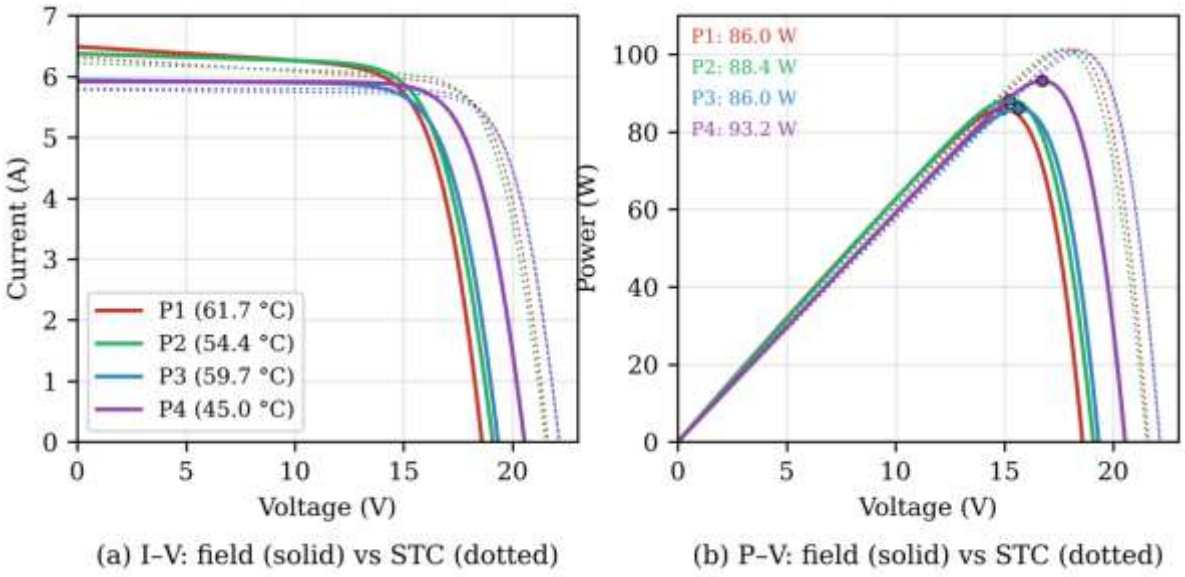


Figure 8: Model II curves at field conditions versus STC.

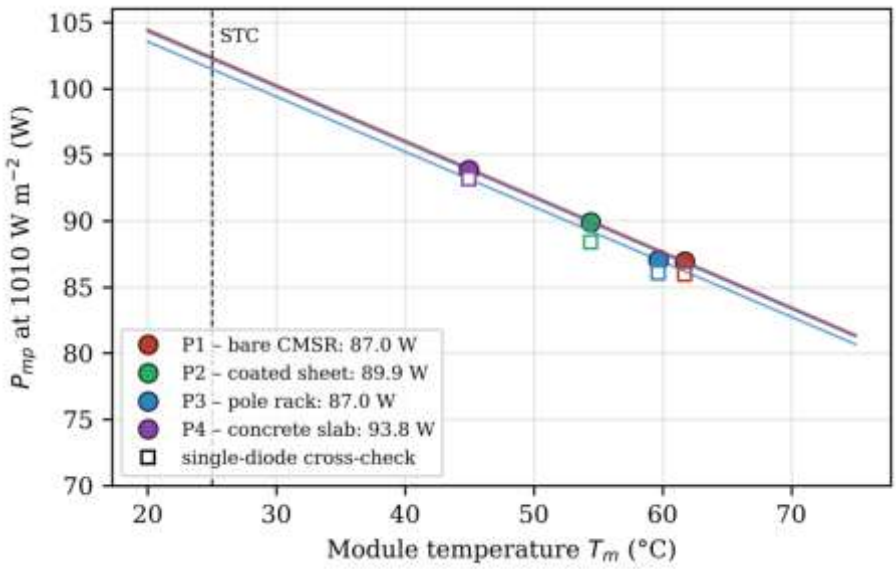


Figure 9: Thermal derating of P_{mp} ($\gamma = -0.41$ % K^{-1}) with field operating points.

3.8 Energy, thermal performance ratio and loss apportionment

Table 8 and Figure 10 summarizes the 3.8 h window. Delivered energy ranged from 330.4 Wh (bare roof) to 356.6 Wh (concrete slab) with Model I, and from 326.7 to 354.0 Wh with Model II. Thermal losses were 15.1,

ISSN 2278-2540 | DOI: 10.51583/IJLTEMAS | Volume XV, Issue XI, November 2026

14.2, 12.1 and 8.2 % (Model I) and 16.0, 15.2, 13.6 and 8.9 % (Model II) for the bare roof, pole, coated sheet and slab. P4 is nominally 0.14 % below P1 at STC but delivered 7.9 % (Model I) to 8.4 % (Model II) more energy. Field-mean efficiency was 14.10 % for P4 against 13.07 % for P1. The two models agree on the ranking and differ by less than 0.5 percentage points in the P4–P1 gap, so the conclusion does not depend on the choice of temperature coefficient. Figure 11a shows that the four modules supplied between 24.3 % and 26.2 % of the total energy despite identical nameplate ratings.

Table 8: Energy performance over the 3.8 h window of Campaign B.

Quantity	**Unit**	**P1**	**P2**	**P3**	**P4†**
Mean power, Model I	W	86.95	89.92	87.05	93.84
Energy, Model I	Wh	330.4	341.7	330.8	356.6
Energy, Model II	Wh	326.7	335.8	327	354
Loss-free reference, E_{ref}	Wh	388.9	388.6	385.5	388.4
Thermal loss, Model I / II	%	15.1 / 16.0	12.1 / 13.6	14.2 / 15.2	8.2 / 8.9
PR_{th}, Model I / II	–	0.849 / 0.840	0.879 / 0.864	0.858 / 0.848	0.918 / 0.911
Field-mean efficiency, Model I	%	13.07	13.51	13.08	14.1
Translated V_{oc}, Model I / II	V	19.01 / 18.60	19.45 / 19.10	19.62 / 19.34	20.71 / 20.55
Energy gain vs P1, Model I / II	%	—	1.21429	1	0.94048

Model I values integrate the minute series; Model II values use mean conditions (G = 1010 W m^{-2}, mean T_m).

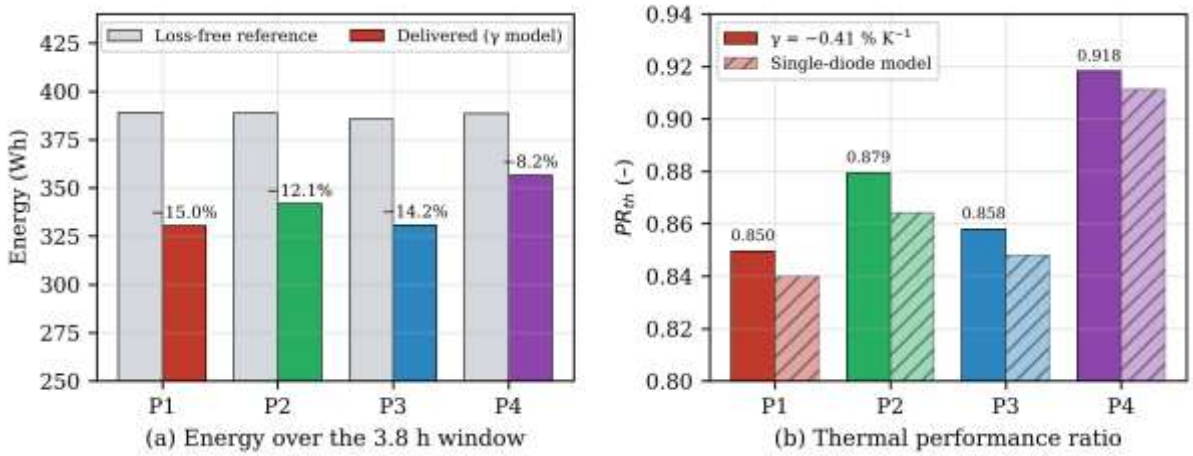


Figure 10: Energy and thermal performance ratio.

ISSN 2278-2540 | DOI: 10.51583/IJLTEMAS | Volume XV, Issue XI, November 2026

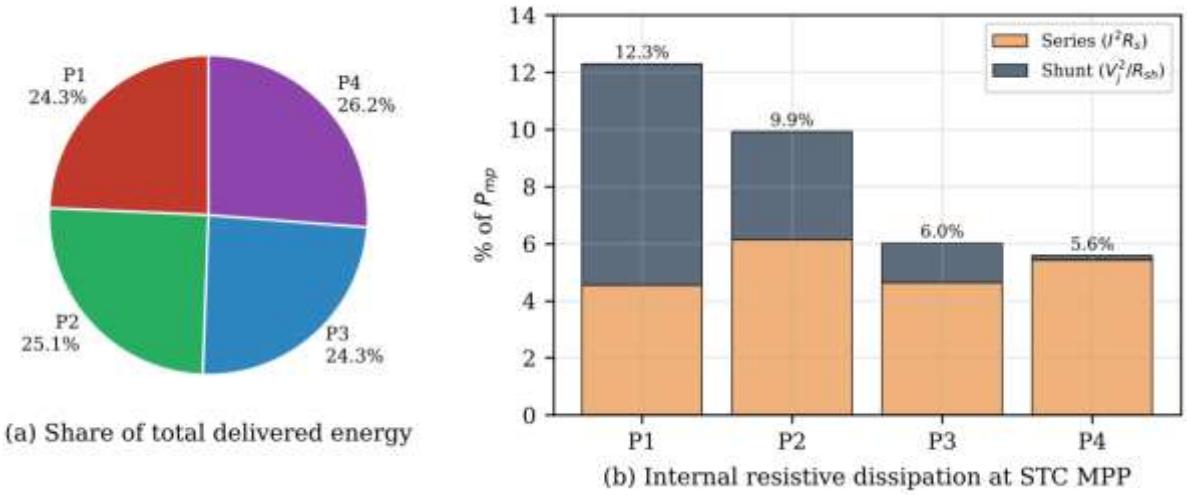


Figure 11: Energy and internal resistive dissipation at STC.

3.9 Roof–module thermal coupling and the paired substrate test

Campaign A (9 February; 1032 ± 6 W m^{-2}, 32.7 ± 2.4 °C ambient) isolates the bare-roof mechanism. The module on the bare sheet averaged 74.7 °C and peaked at 80.3 °C, above the 70 °C 98th-percentile threshold that IEC TS 63126 uses to require higher-temperature qualification (IEC, 2025; Kempe et al., 2023). The exposed sheet averaged 67.4 °C, while the sheet in the module's shadow averaged 58.7 °C. That 8.6 K difference indicates that the array also shades the roof and reduces heat gain into the building below.

Campaign C is the cleanest comparison in the data set because the coated-sheet and concrete-slab modules were logged simultaneously with identical instruments. The minute-wise paired difference was 10.34 ± 2.26 K in favour of the slab over 229 common minutes (10.91 K over the full 357 min). The 95 % confidence interval is 10.0–10.6 K if minutes are treated as independent and 8.9–11.8 K at n_{eff} = 12. Even under conservative assumptions, the slab installation ran at least about 9 K cooler. Module identity remains confounded with substrate here as well.

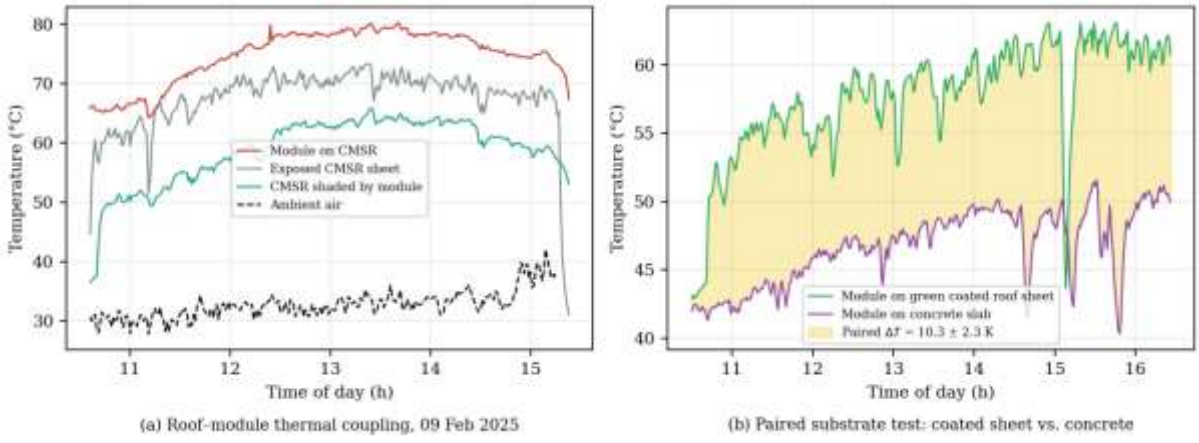


Figure 12: Roof module thermal coupling and paired coated-sheet versus slab test.

4. DISCUSSION

Module–substrate pairs differ more than module ratings. The four modules differ by less than 1 % in STC power and by 0.13 percentage points in efficiency, yet their modelled energy differed by up to 7.9–8.4 %. The direction of the main contrasts – bare metal roof hottest, concrete slab coolest – is physically expected and, for the slab, independently confirmed by the paired test. Their magnitude cannot be attributed to the substrate alone, because each module occupied a single substrate and modules from different manufacturers can differ in back-sheet absorptance, frame design and laminate construction. The effect is larger than the 2.27 % yield

ISSN 2278-2540 | DOI: 10.51583/IJLTEMAS | Volume XV, Issue XI, November 2026

difference reported by Yadav et al. (2025) for rooftop versus simulated ground-mounted arrays, and larger than the roughly 3 % sensitivity to heat-loss factors reported by Pretorius and Nielsen (2024). That is plausible for a close-coupled hot metal back-plane, but it should be confirmed by replication.

Back-plane radiative properties matter. The 7.3 K difference between the bare and coated sheets, which share the same geometry and standoff, points to the radiative environment behind the module. Galvanized steel absorbs strongly relative to its low thermal emittance, so it runs hot; its low emittance also reflects much of the module's rear-face infrared emission back to the laminate. A painted sheet has high emittance: it exchanges radiation efficiently and runs cooler. Coating or painting the roof area beneath a close-coupled array with a high-emittance, high-reflectance finish is therefore a low-cost intervention worth testing directly. The 7.3 K figure is an upper estimate of its benefit, because it also includes any difference between modules P1 and P2.

The pole-mount anomaly. The result for the pole rack contradicts both theory and the literature and is not consistent with the response of the P3 series to transient events. It should not be used to argue that open racks lose their advantage at altitude. A repeat measurement with cross-calibrated sensors, verified attachment and anemometry is required.

Datasheet NOCT is not an installation design tool. NOCT is defined for an open rack and cannot encode the substrate. Yield simulations that use datasheet NOCT will misestimate temperature for other installations, and site- or configuration-specific heat-loss coefficients (k_R or U_0, U_1) are preferable (Pretorius & Nielsen, 2024).

Device-level implications. When a common ideality factor is used, P1's low fill factor arises mainly from a

low shunt resistance (45 Ω), not from high series resistance. Low shunt resistance costs proportionally more at low irradiance, so a procurement specification for small tropical systems could usefully state a minimum fill factor (about 78 % is achievable, as P3 and P4 show) alongside nameplate power. These parameters were derived from rounded datasheet values and should be confirmed with measured I–V curves.

Economic framing. Over the 3.8 h window, the slab-mounted module produced 26.2 Wh more than the bare-roof module, about 0.26 kWh per kWp. Scaled to a full clear-sky day, the difference is of order 0.40–0.50 kWh per kWp; every 100 such days would add 40–50 kWh per kWp. An annual estimate requires the local frequency of clear-sky days and measurements across seasons, which this study does not provide.

5. LIMITATIONS

- **Confounding of module and substrate.** One module per configuration, with no rotation of assignments, means module-to-module and sensor-to-sensor differences cannot be separated from the substrate effect. Replication with rotated assignments is the most important next step.

- **Electrical output.** No I–V tracer or MPP load was used. Power, energy, efficiency and PR_{th} are thermal-derating projections from datasheet values; agreement between Models I and II shows that the relative comparison is insensitive to the choice of coefficients.

- **Wind speed.** No anemometer was installed, so wind speed and direction were not recorded. The Ross coefficients, heat-loss coefficients and field NOCT values of Table 7 are therefore conditional on the prevailing, unmeasured wind; the wind speed quoted in Section 3.6 is inferred from the Faiman model rather than measured; and the 13:03 cooling event of 10 February cannot be attributed to a gust with certainty.

These limitations cannot be removed by re-analysing the present data set; they require new measurements. A follow-up campaign is therefore proposed with: (i) at least two modules of each type, rotated among the four substrates in a Latin-square schedule so that each module occupies each substrate on at least three clear-sky days, allowing module, substrate and day effects to be separated with a mixed-effects model; (ii) measured

ISSN 2278-2540 | DOI: 10.51583/IJLTEMAS | Volume XV, Issue XI, November 2026

electrical output for every module, using an I–V tracer at 5–10 min intervals and an MPP-tracking electronic load logged between sweeps, to validate Models I and II directly; (iii) a cup or ultrasonic anemometer and wind vane at module height logged at 1 min, so that the Faiman coefficients U_0 and U_1 can be fitted for each substrate; and (iv) cross-calibrated back-surface sensors and a coplanar pyranometer.

6. CONCLUSIONS

Four 100 W polycrystalline modules on four substrates were monitored in Arusha (1 400 m) under clear-sky conditions in February 2025. The principal findings are:

- Under about 1010 W m^{-2} and 31.2 °C ambient, mean module temperatures were 61.7 °C (bare CMSR), 59.7 °C (pole), 54.4 °C (coated sheet) and 45.0 °C (concrete, reconstructed), a spread of 16.7 K between module–substrate pairs.

- The synchronous paired test showed the concrete-slab module running 10.3 K cooler than the coated-sheet module (95 % CI 8.9–11.8 K under conservative autocorrelation assumptions). The bare-roof versus coated-sheet contrast (7.3 K) is also robust.

- Thermal losses were 15.1, 14.2, 12.1 and 8.2 % ($\gamma = -0.41$ % K^{-1}), and the slab installation delivered 7.9–8.4 % more energy than the bare-roof installation across two independent translation models.

- Field-effective NOCT was 1.9–16.1 K below the declared 46–47 °C; datasheet NOCT does not describe the installation.

- With a consistent single-diode extraction, the fill-factor deficit of the lowest-ranked module is shunt-dominated ($R_{sh} = 45\ \Omega$), implying a larger penalty at low irradiance.

In tropical highland settings the mounting substrate, and in particular the radiative properties of a close-coupled roof back-plane, should be treated as a design variable alongside module selection. Where close-roof mounting is unavoidable, a high-emittance coating beneath the array, a larger standoff or a reflective intermediate layer are low-cost options that warrant controlled testing. Future work should use several modules per configuration with rotated assignments, cross-calibrated sensors, a verified coplanar pyranometer, anemometry, I–V tracing and a full annual cycle.

Declaration of competing interest

The authors declare no competing financial or non-financial interests.

REFERENCES

1. Adamu, H., Njoka, F., & Kidegho, G. (2024). Performance of MPPT charge controller under moderate- to high-temperature field conditions. *Journal of Sustainable Development of Energy, Water and Environment Systems, 12*(3), Article 1120504. https://doi.org/10.13044/j.sdewes.d12.0504
2. Duffie, J. A., Beckman, W. A., & Blair, N. (2020). *Solar engineering of thermal processes, photovoltaics and wind* (5th ed.). John Wiley & Sons.
3. Dwivedi, P., Sudhakar, K., Soni, A., Solomin, E., & Kirpichnikova, I. (2020). Advanced cooling techniques of P.V. modules: A state of art. *Case Studies in Thermal Engineering, 21*, Article 100674. https://doi.org/10.1016/j.csite.2020.100674
4. Holmgren, W. F., Hansen, C. W., & Mikofski, M. A. (2018). pvlib python: A python package for modeling solar energy systems. *Journal of Open Source Software, 3*(29), 884. https://doi.org/10.21105/joss.00884
5. International Electrotechnical Commission. (2016). *Photovoltaic (PV) module performance testing and energy rating – Part 2: Spectral responsivity, incidence angle and module operating temperature measurements* (IEC 61853-2). IEC.

ISSN 2278-2540 | DOI: 10.51583/IJLTEMAS | Volume XV, Issue XI, November 2026

6. International Electrotechnical Commission. (2021a). *Photovoltaic devices – Procedures for temperature and irradiance corrections to measured I–V characteristics* (IEC 60891, 3rd ed.). IEC.
7. International Electrotechnical Commission. (2021b). *Photovoltaic system performance – Part 1: Monitoring* (IEC 61724-1). IEC.
8. International Electrotechnical Commission. (2025). *Guidelines for qualifying PV modules, components and materials for operation at high temperatures* (IEC TS 63126, 2nd ed.). IEC.
9. Kaplanis, S., Kaplani, E., & Kaldellis, J. K. (2022). PV temperature and performance prediction in free-standing, BIPV and BAPV incorporating the effect of temperature and inclination on the heat transfer coefficients and the impact of wind, efficiency and ageing. *Renewable Energy, 181*, 235–249. https://doi.org/10.1016/j.renene.2021.08.124
10. Kempe, M. D., Ovaitt, S., Springer, M., Brown, M., Jordan, D., Sekulic, W., O'Brien, C., Jaubert, J.-N., Yu, Y., Oh, J., TamizhMani, G., & Li, B. (2023). Close roof mounted system temperature estimation for compliance to IEC TS 63126. In *Proceedings of the 50th IEEE Photovoltaic Specialists Conference (PVSC)*. IEEE.
11. Kurnia, A. M. (2026). Comparative analysis of temperature coefficients and thermal performance degradation of 50 WP monocrystalline and polycrystalline solar panels using artificial radiation simulation. *Asian Journal of Applied Education, 5*(2), 367–382. https://doi.org/10.55927/ajae.v5i2.16492
12. Lazarus, E., Lewis, D. J., Stock, J. H., & Watson, M. W. (2018). HAR inference: Recommendations for practice. *Journal of Business & Economic Statistics, 36*(4), 541–559. https://doi.org/10.1080/07350015.2018.1506926
13. Lo Brano, V. (2026). Open and reproducible estimation of PV single-diode parameters from datasheet data. *Energy Reports, 15*, Article 109280. https://doi.org/10.1016/j.egyr.2026.109280
14. Malik, P., Chandel, S. S., & Gupta, R. (2025). A comprehensive review on future research trends in solar cell parameter extraction techniques. *Renewable Energy, 251*.
15. Mlazi, N. J., Mayengo, M., Lyakurwa, G., & Kichonge, B. (2024). Mathematical modeling and extraction of parameters of solar photovoltaic module based on modified Newton–Raphson method. *Results in Physics, 57*, Article 107364. https://doi.org/10.1016/j.rinp.2024.107364
16. Mohamad Radzi, P. N. L., Mekhilef, S., Mohamed Shah, N., Akhter, M. N., Hassani, S., Albaker, A., & Wahyudie, A. (2025). Performance evaluation and degradation analysis of grid connected photovoltaic systems for energy efficient buildings in tropical climates. *Scientific Reports, 15*, Article 39103. https://doi.org/10.1038/s41598-025-26765-9
17. Oezkalay, E., Friesen, G., Caccivio, M., Bonomo, P., Fairbrother, A., Virtuani, A., & Ballif, C. (2022). Operating temperatures and diurnal temperature variations of modules installed in open-rack and typical BIPV configurations. *IEEE Journal of Photovoltaics, 12*(1), 133–140. https://doi.org/10.1109/JPHOTOV.2021.3114988
18. Ogbomo, O. O., Amalu, E. H., Ekere, N. N., & Olagbegi, P. O. (2017). A review of photovoltaic module technologies for increased performance in tropical climate. *Renewable and Sustainable Energy Reviews, 75*, 1225–1238. https://doi.org/10.1016/j.rser.2016.11.109
19. Pretorius, J., & Nielsen, S. (2024). Understanding heat dissipation factors for fixed-tilt and single-axis tracked open-rack photovoltaic modules: Experimental insights. *Progress in Photovoltaics: Research and Applications*. https://doi.org/10.1002/pip.3852
20. Prilliman, M., Stein, J. S., Riley, D., & Tamizhmani, G. (2020). Transient weighted moving-average model of photovoltaic module back-surface temperature. *IEEE Journal of Photovoltaics, 10*(4), 1053–1060. https://doi.org/10.1109/JPHOTOV.2020.2992351
21. Rajani, A., Mat Said, D., Ahmad Noorden, Z., Ahmad, N., Arifin, M. S., Atmaja, T. D., Suryaman, N. N., Mustapha, M., Muzhaffar, H. A., Fudholi, A., & Saputra, R. E. (2026). Electrical and thermal performance of double-pass bifacial photovoltaic thermal system in tropical climate. *Case Studies in Thermal Engineering*, Article 107760. https://doi.org/10.1016/j.csite.2026.107760
22. Santiago, I., Trillo-Montero, D., Moreno-Garcia, I. M., Pallarés-López, V., & Luna-Rodríguez, J. J. (2018). Modeling of photovoltaic cell temperature losses: A review and a practice case in South Spain. *Renewable and Sustainable Energy Reviews, 90*, 70–89. https://doi.org/10.1016/j.rser.2018.03.054
23. Smets, A., Jäger, K., Isabella, O., van Swaaij, R., & Zeman, M. (2016). *Solar energy: The physics and engineering of photovoltaic conversion technologies and systems*. UIT Cambridge.

ISSN 2278-2540 | DOI: 10.51583/IJLTEMAS | Volume XV, Issue XI, November 2026

24. Wilks, D. S. (2019). *Statistical methods in the atmospheric sciences* (4th ed.). Elsevier.
25. Yadav, D., Yadav, S. K., Varma, V., Khatoon, S., Singh, J., Singh, R. B., Hasnain, S. M. M., Paramasivam, P., & Tufa, M. A. (2025). Experimental analysis of elevated temperature and soiling loss on the rooftop PV modules performance under composite climatic conditions. *Scientific Reports, 15*, Article 42035. https://doi.org/10.1038/s41598-025-25846-z